Celal Bayar University Journal of Science

Self-tuning Fuzzy PID Controller Design and Energy Management in DC Microgrid: Standalone and Grid Connected Mode

Ahmet Kaysal[1]* (iD), Selim Köroğlu[2] (iD), Yüksel Oğuz[3] (iD)

[1]Department of Electrical Engineering, Afyon Kocatepe University, Afyonkarahisar, Turkey.
[2]Department of Electrical Electronics Engineering, Pamukkale University, Denizli, Turkey.
[3]Department of Electrical Electronics Engineering, Afyon Kocatepe University, Afyonkarahisar, Turkey.
*akaysal@aku.edu.tr
*Orcid: 0000-0002-4142-0840

Abstract

This paper presents a control system and energy management strategy (EMS) with a standalone and grid-connected mode in the microgrid. The microgrid is energized by distributed energy resources (DER) such as photovoltaic panels, wind turbines and lithium-ion batteries. The controller structure for regulating the voltage regulation in this microgrid consisting of renewable energy sources and an energy storage system is covered. Overshoot, rise time, settling time performances of designed self-tuning fuzzy proportional-integral-derivative (SFPID) controller and conventional proportional-integral-derivative (PID) controller examined comparatively. In addition, an EMS has been proposed for loads that fed in the microgrid. Here, the aim is to make maximum use of RESs as much as possible, maintain voltage regulation, and ensure continuity in the feeding of the critical load. The system switches between the standalone and grid-connected modes if necessary. A model of the microgrid's dynamic behavior is constructed, and it is simulated in the MATLAB®/Simulink environment. The proposed SFPID controller stabilizes the bus voltage and frequency oscillations within the allowable tolerance limits in a short time despite the disturbance effects on the generation and load side.

Keywords: Energy management system, fuzzy controller, microgrid, renewable energy system.

1 Introduction

In traditional power systems, energy production methods are largely based on fossil fuels, and the negative effects of these fuels on the environment have become quite alarming. In these systems, central power plants are preferred to meet the energy needs of consumers, and the network structure is interconnected. Therefore, high voltage transmission lines are required during the transmission of energy to the consumption centers. This is the reason for investment costs increase and transmission losses. The production of clean energy in distributed energy resources (DER) based on renewable energy systems (RES), such as photovoltaics (PV) and wind energy (WT), plays an important role due to the positive impact on the environment [1, 2]. In recent years, microgrid (MG) structures fed with alternative energy sources have been raised. The MG system has efficiency, ease of control, and network integration.

MGs are small community networks, and they have attracted much attention in recent years due to their advantages, such as reducing power losses in transmission lines, achieving maximum utilization from RES, and providing reliable energy to consumers. Typical MGs include PV arrays, WTs, energy storage systems (ESS), power DC/DC converters, DC/AC inverters, and local loads that can operate standalone or grid-connected mode in power systems [3]. MGs, which can operate both connected to the main grid and independent of the grid, have proven to be efficient in eliminating the negative effects of intermittent energy generation depending on weather and environmental conditions [4].

MGs are vital for managing existing energy sources, frequency and voltage control, and the smooth and optimum operation of the existing network. In an energy system, it is necessary to keep the amplitudes of the voltage of the load buses within certain operating limits in both steady-state and transient voltage stability events. In the literature, many methods such as fuzzy

logic controller [5], self-tuning fuzzy PI/PID (SFPID) controller [6-9], adaptive neuro-fuzzy controller [10], conventional PID controller [11], predictive power and voltage control [12, 13] are recommended for voltage control in MG. In addition, energy management and optimization have become the focus of research conducted on MGs. The control methods used in the optimum operation of MGs can generally be grouped into four classes such as centralized [14], decentralized [15], distributed and hierarchical control methods [16-18]. Three-level hierarchical control methodology is widely used, including primary, secondary and tertiary control levels [19, 20]. Ziouani et al. [21], a control strategy based on a hierarchical approach, is presented to operate MG, which continuously switches between island mode and grid-connected modes. In order to regulate the output voltage, the inner control is used to improve the stability in the primary control, amplitude, and frequency for active and reactive power-sharing. Mohamed et al. [22] developed a tertiary control algorithm for DC MG, and a laboratory-scale test was performed experimentally.

In this paper, the SFPID controller has been suggested to minimize voltage oscillations in a MG consisting of RES and ESS and improve the voltage response of the system. The designed controller is compared with the conventional PID controller. Furthermore, an energy management strategy (EMS) has been proposed to regulate power flow in MG. The suggested EMS ensures that the voltage and frequency in the MG are maintained at the specified limits and switches between the standalone and the grid-connected modes to ensure continuity in the supply of the critical load.

2 Configuration and Modeling of the Microgrid

PV arrays and WTs based on permanent magnet synchronous generators (PMSG) form renewable energy sources in the MG structure. A battery pack is available to provide the needed power in cases where the generated power cannot meet the load demand. Also, MG includes power electronic converters and dynamic loads used as interfaces in connecting these sources to the DC bus. These components are connected through a DC bus, as shown in Figure 1.

A 400V DC bus is created for RES and ESS. A converter is used when connecting the PV system to the DC bus. The wind turbine based on a PMSG is first converted to DC with the help of a three-phase rectifier and then connected to the DC bus via the boost converter. Here, taking changes in bus voltage and power as a reference and with the control of the boost converter, RES is worked at the maximum power point (MPP). The ESS is connected to the DC bus via the

bidirectional converter to perform charging and discharging according to the state of the energy. The SFPID controller has been suggested to minimize voltage oscillations between MG and AC loads and improve the system's voltage response. The EMS's integration among source, load, and network is carried out according to the priority of the loads. If the resources are insufficient to feed the critical load, the grid-connected mode is switched.

In the suggested MG structure, the total load is 9 kW and the critical power (P_{cr}) is defined as 2.5 kW, load2 (P_{L2}) 3.5 kW and load3 (P_{L3}) 3 kW. The installed power capacity of the system is a total of 11.1 kW, including PV generation system 6.1 kW and WT generation system 5 kW. The energy capacity of the ESS unit used as a storage device in the system is determined as 6 kWh.

2.1. Photovoltaic System

PV systems are one of the most important RES and convert irradiant energy directly into electrical energy. Since the electrical energy obtained from the PV system will vary depending on the sun's position, clouds and temperature changes, the operation of PV arrays at the MPP is important for system efficiency. In the boost converter structure, perturb and observe (P&O) technique provides working at the MPP. Figure 2 shows the boost converter structure, and Table 1 shows the electrical characteristic of the PV module.

Table 1. Electrical characteristics of the photovoltaic module (25 ℃ and 1000 W/m^2).

Description	Symbol	Value
Maximum power (W)	P_{max}	305.23
Open circuit voltage (V)	V_{oc}	64.2
Voltage at MPP (V)	V_{mpp}	54.7
Cells per module	N_{cell}	96
Short-circuit (A)	I_{sc}	5.96
Current at MPP (A)	I_{mpp}	5.58
Diode saturation current (A)	I_0	1.36e^{-11}
Shunt resistance (Ω)	R_{sh}	420.55
Series resistance (Ω)	R_s	0.3778

The PV system consists of 20 modules, five parallel strings and four serial modules per string. As seen in the relationship between the P-V and I-V curves of the PV arrays in Figure 3, the installed capacity of the PV arrays is 25 ℃ cell temperature and 6105 W in the irradiance of 1 kW/m^2. The output voltage of the PV arrays from 218.8 V is increased to 400 V DC bus voltage with the boost converter.
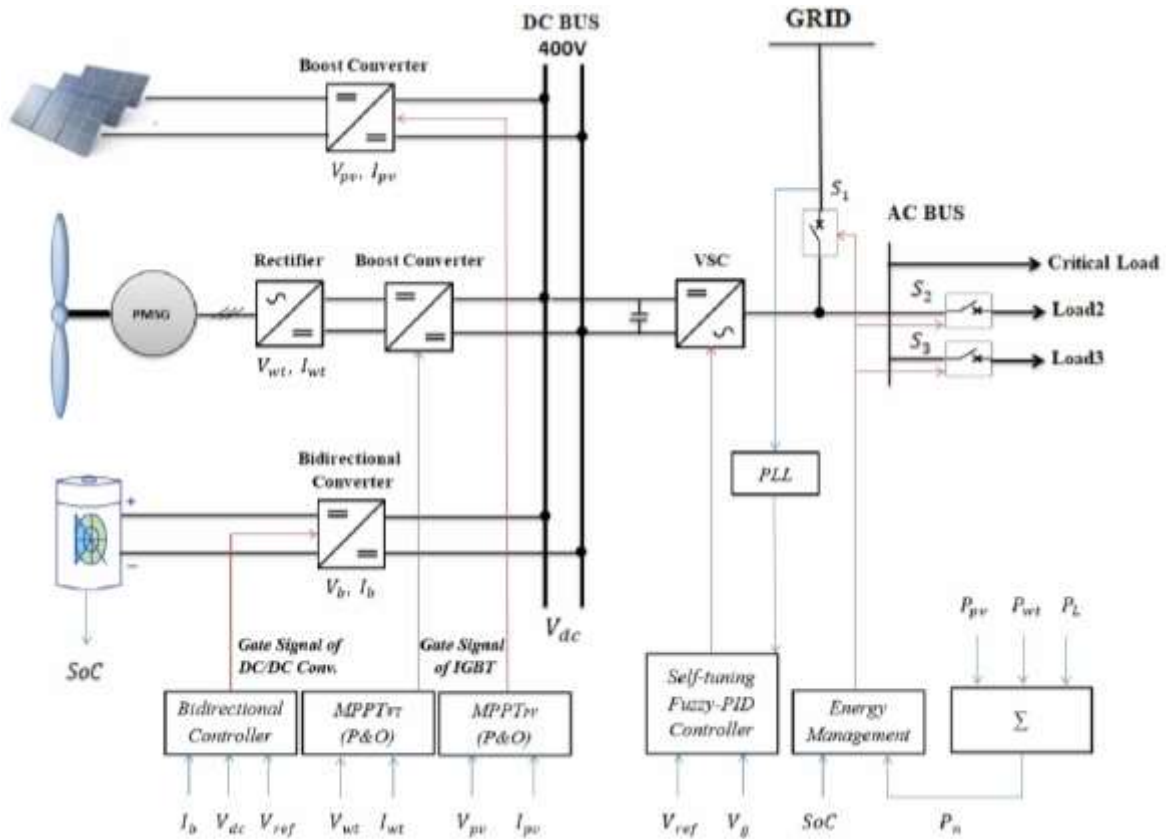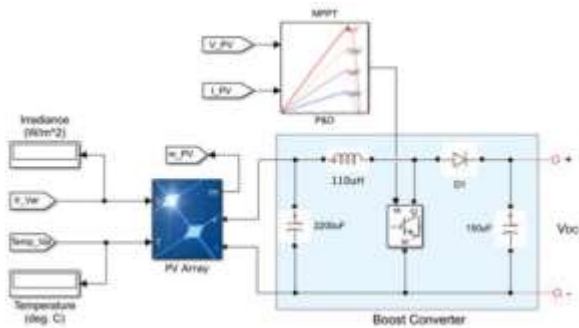
Figure 1. Microgrid power system architecture.

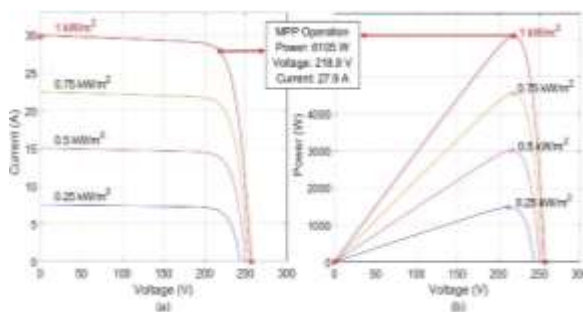**Figure 2.** PV array and boost converter structure.

Figure 3. (a) I-V and (b) P-V curves of the solar simulator in 1 kW/m^2 irradiation.

2.2. Wind Energy System

One of the other essential RES is wind turbines. Many types of generators are used in wind turbines. One of them is PMSGs, which can be used directly in wind turbines without a gear system. For this generator type, the rotor magnetic flux is generated by permanent magnets; therefore, it has no brush mechanism. Since there are no rotor windings, there are no winding losses, and a high-power density can be achieved [23]. The WT, diode rectifier and MPPT controlled converter structure are shown in Figure 4. The technical characteristics of the PMSG are listed in Table 2.
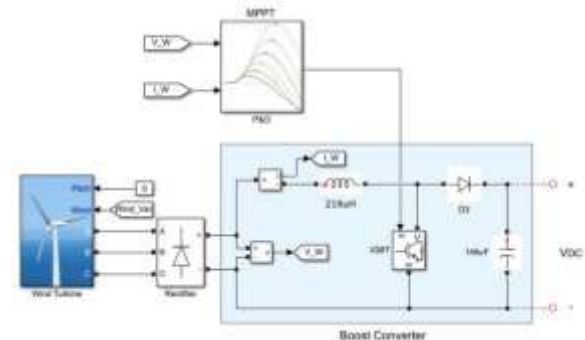

Figure 4. Wind turbine and boost converter structure.

Table 2. Technical characteristics of the PMSG.

Description	Symbol	Value
Nominal PMSG power (W)	P_n	5000
Nominal voltage (L-L) (V)	V_n	425
Stator resistance (Ω)	R_s	0.0918
Stator inductance (mH)	L_s	0.975
No. of pole pairs	p	4
Flux linkage (V.s)	ϕ_f	0.1688
Viscous damping (N.m.s)	F	0.0004924
Moment of inertia (kg. m^2)	J	0.003945

Table 3. Technical specifications of the ESS.

Description	Symbol	Value
Maximum capacity (Ah)	Q	30
Nominal voltage (V)	V_n	200
Fully charged voltage (V)	V_f	232.8
Cut-off voltage (V)	V_c	150
Internal resistance (Ω)	R_i	0.0667
Nominal discharge current (A)	I_d	13.04

2.3. Energy Storage System

The ESS is connected to MG's DC bus with a bidirectional converter. The energy surplus obtained from RES and not used on the load side is stored in ESS. Energy stored is used to meet the demand of the load when the network is not sufficient or the network is not available. Thus, both the critical loads are not de-energized, and the control of the voltage and frequency components is provided within limits. According to the Coulomb Counting method, SOC is given in Equation (2.1).

$$SOC(t) = SOC(t-1) + \int_0^t \frac{I_b}{C_b} dt \qquad (2.1)$$

Where $SOC(t-1)$ is the initial value of SOC right before I_b battery current is applied to the battery cell, C_b is the capacity of the battery and time t of the battery. Charging the battery is performed according to the limits determined in the control algorithm. These limits are important for the safety of the battery and are given in Equation (2.2).

$$SOC_{min} \leq SOC \leq SOC_{max} \qquad (2.2)$$

SOC_{min} and SOC_{max} are the minimum and maximum charge states of the battery. These values are determined as 20% and 100%, respectively. The ESS structure is given in Figure 5, and the used system's technical characteristics are given in Table 3.
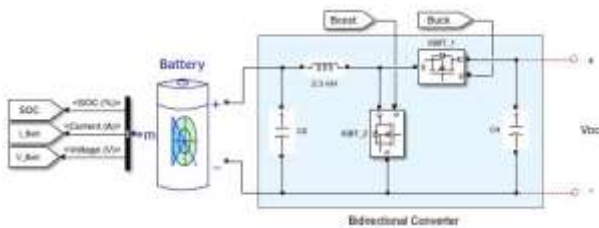

Figure 5. Battery and bidirectional converter structure.

3. Voltage Source Converter and SFPID controller

The voltage source converter (VSC) converts the DC input voltage to a symmetrical AC output voltage at the desired amplitude and frequency. The inverter gain, also known as the modulation index, can be defined as the ratio of the AC output voltage to the DC input voltage [24]. The adjustable output voltage is obtained by controlling this gain parameter in the inverter with the suggested SFPID. The block diagram based on the SFPID controller is given in Figure 6.
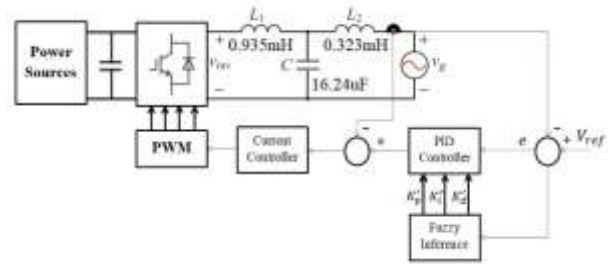

Figure 6. Block diagram of SFPID controller.

The feedback error of the fuzzy inference system is e and the derivative of the error is Δe. They are given in Equations (3.1) and (3.2).

$$e(t) = V_{ref}(t) - V_g(t) \qquad (3.1)$$

$$\Delta e(t) = e(t) - e(t-1) \qquad (3.2)$$

Where $V_{ref}(t)$ represents reference input, $V_g(t)$ represents output signal. Feedback error e and Gaussian membership functions are used during the fuzzification of the derivative of the error Δe, and it is represented in Equation (3.3) [25].

$$f(x; \sigma, c) = exp\left(-\frac{(c-x)^2}{2\sigma^2}\right) \qquad (3.3)$$

Where the width of the fuzzy set is σ and the center of fuzzy set c. Thus, the input data e and Δe are converted to the appropriate linguistic value using the fuzzy Mamdani inference model. The fuzzy inference system linguistic variables are organized as negative big (N$_{BB}$),

positive big (PBB), negative small (NSS), positive small (PSS) and zero (ZR). Rule bases are given in Table 4, and Table 5 and membership functions for input and output variables are given in Figure 7. In the next step of the fuzzy inference system, K_p', K_d' and K_i' outputs are determined according to the rule base defined in Table 4 and Table 5. As an example;

IF e(t) is NBB and Δe(t) is ZR THEN K_p is PSS, K_d is NSS and K_i is NSS. All other cases are described similarly.

Table 4. The rule base of K_p and K_d

e \ Δe	NBB	NSS	ZR	PSS	PBB
NBB	PBB	PBB	PSS	PSS	ZR
NSS	PBB	PSS	ZR	ZR	NSS
ZR	PBB	ZR	ZR	ZR	NBB
PSS	PSS	ZR	ZR	NSS	NBB
PBB	ZR	NSS	NSS	NBB	NBB

Table 5. The rule base of K_i

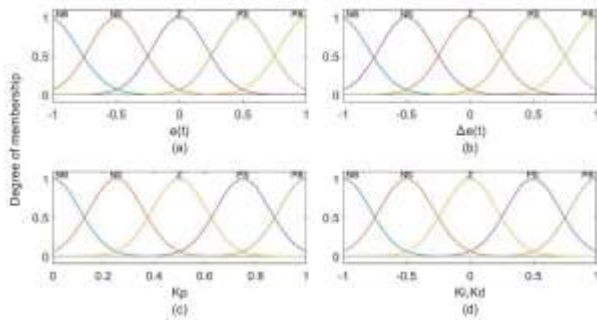| e \ Δe	NBB	NSS	Z	PSS	PBB
NBB	NBB	NBB	NSS	NSS	ZR
NSS	NBB	NSS	ZR	ZR	PSS
ZR	NBB	ZR	ZR	ZR	PBB
PSS	NSS	ZR	ZR	PSS	PBB
PBB	ZR	PSS	PSS	PBB	PBB

Figure 7. Gaussian membership functions for input variable (a) $e(t)$ (b) $\Delta e(t)$ and output variable (c) K_p gain (d) K_i and K_d gain.

Finally, the fuzzy output is converted to a sharp control signal in the defuzzification process. The centroid method defined in Equation (3.4) is used during this process.

$$x = \frac{\sum_{i=1}^{n} x_i \cdot \mu(x_i)}{\sum_{i=1}^{n} \mu(x_i)} \qquad (3.4)$$

Where, x is the defuzzified value, x_i indicates the sample element, $\mu(x_i)$ is the membership function,

and n represents the number of elements in the sample. Thus, the best proportional gain constant K_p', the integral gain constant K_i' and derivate gain constant K_d' outputs are obtained. These values are used as the multiplier in the calculation of PID coefficients. According to Equation (3.5)-(3.7), the PID controller parameters are updated.

$$K_p = K_{p0} * K_p' \qquad (3.5)$$

$$K_i = K_{i0} * K_i' \qquad (3.6)$$

$$K_d = K_{d0} * K_d' \qquad (3.7)$$

Where, K_p' is proportional modification coefficient, K_i' is integral modification coefficient, K_d' is derivative modification coefficient. The initial values of the PID controller are calculated using transfer function-based Simulink PID Tuner. K_{p0} is initial proportional gain (0.02), K_{i0} is initial integral gain (0.6), and K_{d0} is initial derivative gain (0.0001). The control signal of the SFPID controller is defined as shown in Equation (3.8). Simulink block diagram of the MG is given in Figure 8.

$$U_{FPID} = K_p e(t) + K_i \int e(t) + K_d \frac{de(t)}{dt} \qquad (3.8)$$

Finally, filtration is performed to bring the voltage at the inverter output closer to the form of a sinusoidal wave. An LCL filter was used for this purpose. As a result of the analyzes, calculated values of inductors L_1 and L_2 and capacitor C are 0.935mH, 0.323mH and 16.24 µF, respectively (see Figure 6).

4. Energy Management System in DC Microgrid

The EMS provides coordination between MG's standalone mode and grid-connected modes. It also allows activation and de-activation of loads in a controlled manner. Depending on the state of the sources and loads, the power equation in MG should be defined as in Equation (4.1).

$$P_{pv} + P_{wd} = P_L \pm P_{batt} \qquad (4.1)$$

Where, the P_{batt} represents battery power, P_{pv}, P_{wd} represent power generated by PV array and WT, respectively. P_L represents the total power of loads that are connected to MG. Similarly, the total load is defined by Equation (4.2).

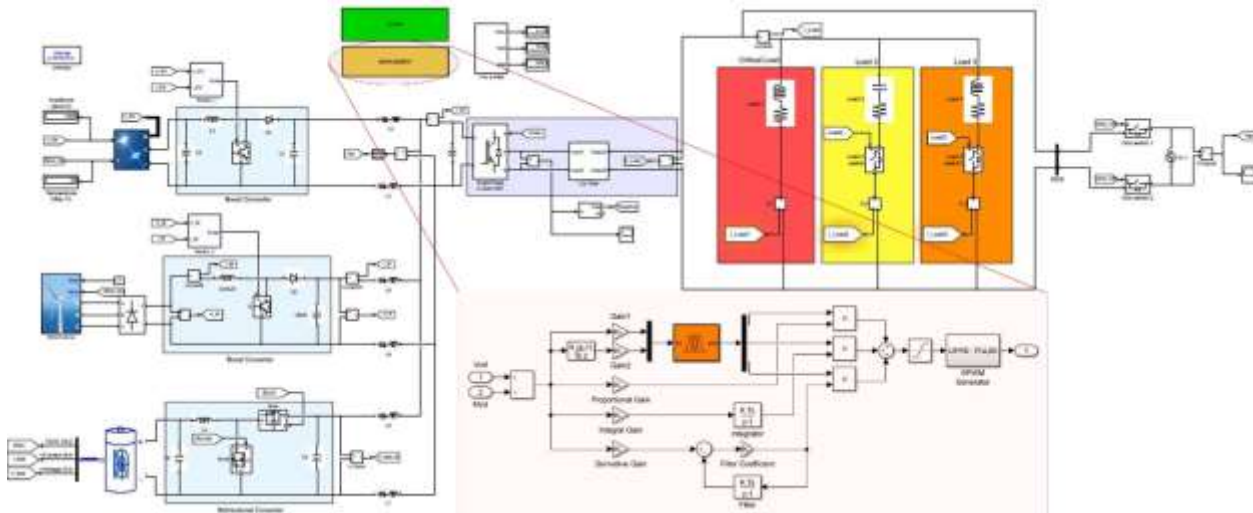$$P_{cr} + P_{L2} + P_{L3} + P_{Loss} = P_L \qquad (4.2)$$

Figure 8. Simulink diagram of the MG architecture.

P_{cr} represents the critical load that must be active continuously. P_{L2} and P_{L3} are loads that can be controlled according to the load condition. The EMS flow diagram between power supplies and loads is shown in Figure 9.

In this case, scenarios related to SOC are given in Table 6. According to the flow diagram, if the total power produced by RES is insufficient to meet the demanded power, the battery supplies the energy as required. If SOC falls below 50%, it opens the S_2 circuit breaker, and so load2 is disabled. If SOC falls below 40%, it opens the S_3 circuit breaker, and so load3 is deactivated.

Table 6. MG transition strategy

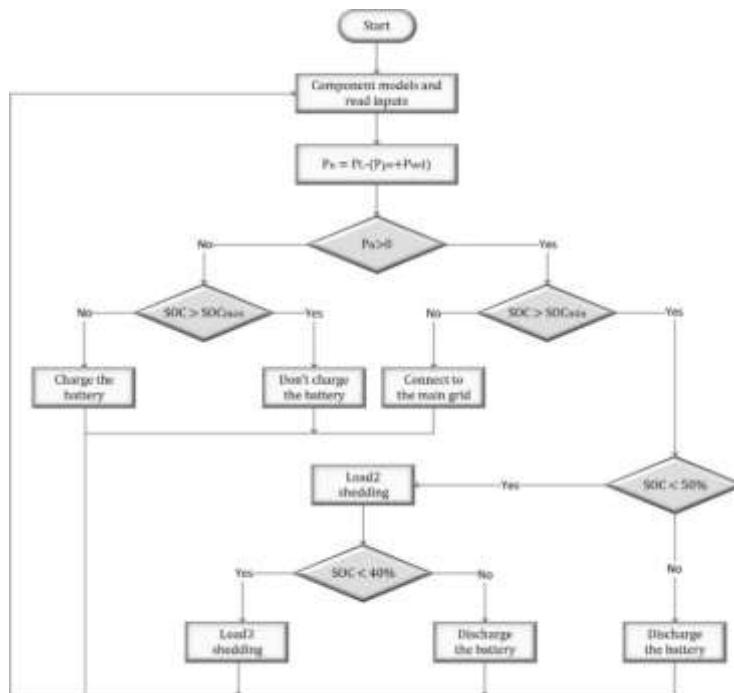| Scenarios	Transition conditions	Events
1	SOC<SOC$_{max}$	Battery discharging, PV and WT are in MPPT
2	SOC<50%	Load2 shedding, PV and WT are in MPPT
3	SOC<40%	Load2 shedding, PV and WT are in MPPT
4	SOC<SOC$_{min}$	Pgrid ⟶ ON
5	SOC>SOC$_{max}$	Pgrid ⟶ OFF

Figure 9. Flowchart of the proposed EMS.

A. Kaysal

If the SOC, which is determined as the safe range for the battery, falls below the SOC_{min} level, the power flow from the battery to the load is stopped. The grid is switched to connected mode, and the battery is charged in this case. If the production capacity of the power supplies is greater than the demanded load, the energy surplus is stored in the battery. When the battery reaches SOC_{max} level, excess energy is transferred to the grid.

5. Simulation Results and Discussion

In Figure 1, the block diagram is simulated in the DC MG MATLAB®/Simulink environment. A SFPID controller is designed for system voltage stability. The comparison of PID and SFPID controllers is given in Figure 10. The performance values for the PID and SFPID controllers are given in Table 7. Reference root mean square (RMS) value of output voltage in MG is 230 V. When a PID controller is used in the control structure of the VSC, the overshoot value of the output voltage is 244 V, and this value is 236 V when the SFPID controller is used. Similarly, for the PID controller, the rise time is 0.035s, and the settling time is 0.301s, while for the SFPID controller, these values are 0.021s and 0.075s, respectively. The results show that the proposed SFPID controller improves the overshoot 57.14%, rise time 40% and settling time 75.08% in performance criteria compared to the PID controller.

Table 7. Comparative performance analysis of PID and SFPID controllers.

Parameter	PID	SFPID
Overshoot (%)	6.087	2.609
Rise Time (s)	0.035	0.021
Settling Time (s)	0.301	0.075

The voltage and frequency stability of the MG on the standalone and grid-connected modes has been analyzed under variable production scenarios. In these scenarios, the solar radiation is 0.2-1 kW/m², and the wind speed is changed autonomously between 8-12 m/s. When the simulation is started, the SOC of the battery is 80%. The changes in the power flow between the source and the load are given in Figure 11. In the initial case, the solar panels produce 6.08 kW in 1 kW/m², the wind turbine produces 5.4 kW at 12 m/s, and the totally produced power is 11.08 kW. In this case, all loads with a total of 9 kW are operational. The surplus 2.26 kW power is transferred to ESS. When solar irradiance decreased to 0.25 kW/m² at second 2, the energy obtained from solar panels decreased to 1.59 kW. In this case, because the power supplies are insufficient to meet the demand power, 2.5 kW of power is met from ESS to meet the total load.

Since the SOC value of the battery falls below 50% of the limit value defined in the EMS in 5 s, load2 with the lowest priority level of 3.5 kW is disabled, and surplus 0.52 kW power is used to charge the ESS. It is assumed that wind speed is to fall to 8 m/s and the solar irradiance is 0.1 kW/m² in the 6th second. Since the power produced under these conditions could not meet the current demand load, the ESS in the charge state went into discharge mode with 4.33 kW power to meet the remaining load demand. When ESS continues discharge for a while, SOC falls below 40%, load3 with low priority was disabled and critical load continued to feed. Discharge operation is stopped because the battery charge falls below SOC_{min} level in the 10.2th second. In order to be ensured of feed of the critical load, EMS switched to grid-connected mode. When the system switches to the grid mode, all loads are supplied, and RES has charged ESS. As the SOC level of ESS reached to SOC_{max} in 14 s, the grid was deactivated and switched back to standalone mode. Thus, the supply of the loads continues to be provided by the RES.

The variation of DC bus current and voltage in MG is given in Figure 12 compared to PID and proposed SFPID controller. Voltage variation in the DC bus is shown in Figure 12 (a) for PID and SFPID controllers. In this system, it is desired that the DC link voltage remains at 400 V. In order to evaluate the change in the DC bus voltage during the simulation process generated in different scenarios, voltage regulation values maximum positive ε_k^+ and lowest negative ε_k^- were obtained according to Equation (5.1) [26].

$$\varepsilon_k^+ = \frac{\overline{u_k} - min(u_k)}{\overline{u_k}}.100\%$$

$$\varepsilon_k^- = \frac{\overline{u_k} - max(u_k)}{\overline{u_k}}.100\%$$

(5.1)

Where, $\overline{u_k}$ is reference DC voltage and u_k is the DC voltage value at the time of operation. Maximum oscillation in the DC bus voltage has occurred in the 14th second due to changes in scenarios or load after the condition in which MG gets into a steady state. As seen in Figure 12 (a), considering the oscillation values that continued for 200 ms in the 14th s, the voltage regulation results obtained from the PID controller are 8.75% and 0% (ε_k^+ and ε_k^-), and the results obtained from the proposed SFPID controller are 4.85% and 0%, respectively. The variation of the DC bus current is shown in Figure 12 (b) for both controllers. Here, the DC current change of the system depending on the load is seen. The fluctuation of the DC bus current is seen to be high at the start. This is due to the voltage and current oscillations during the wind turbine operation.
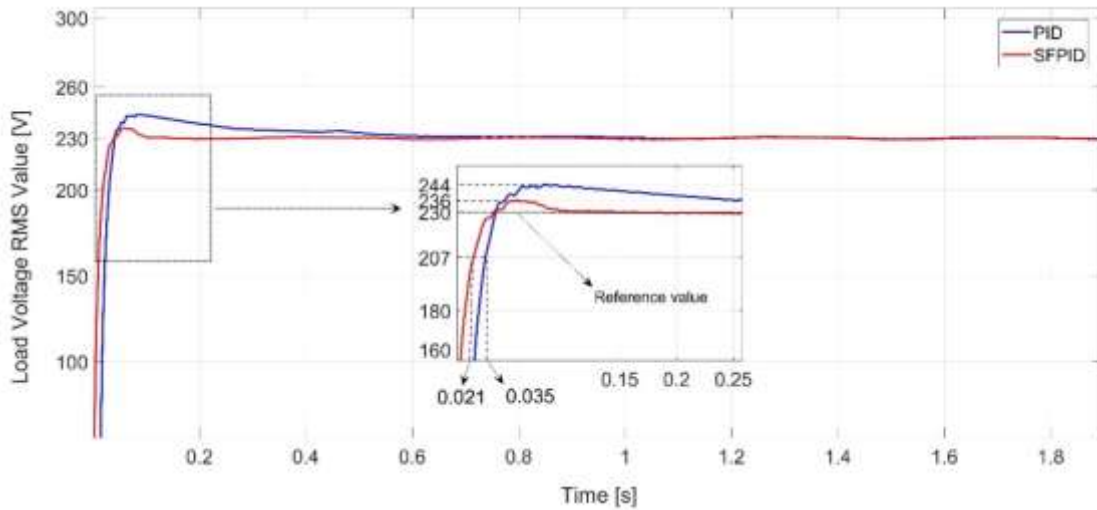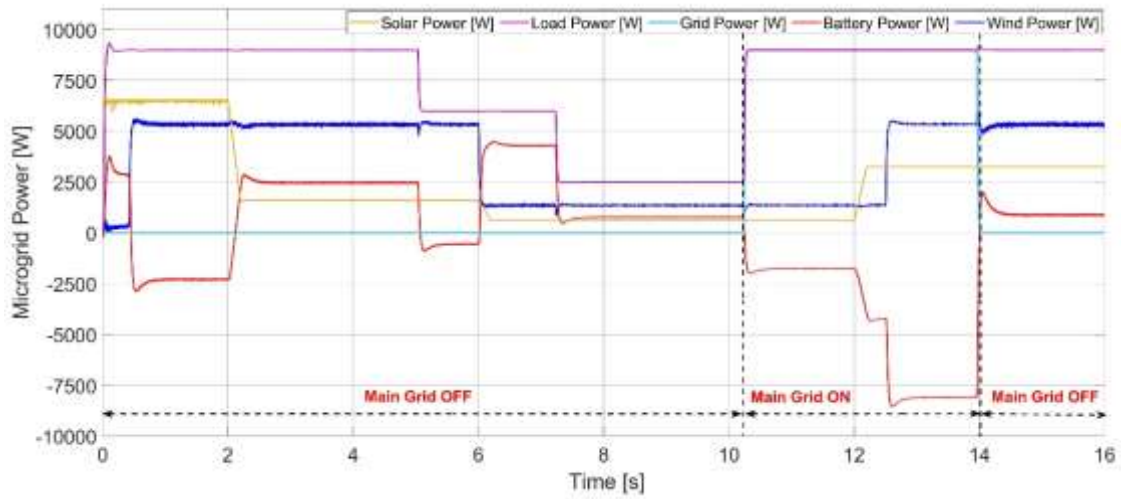
Figure 10. Comparative graphic of control methods.

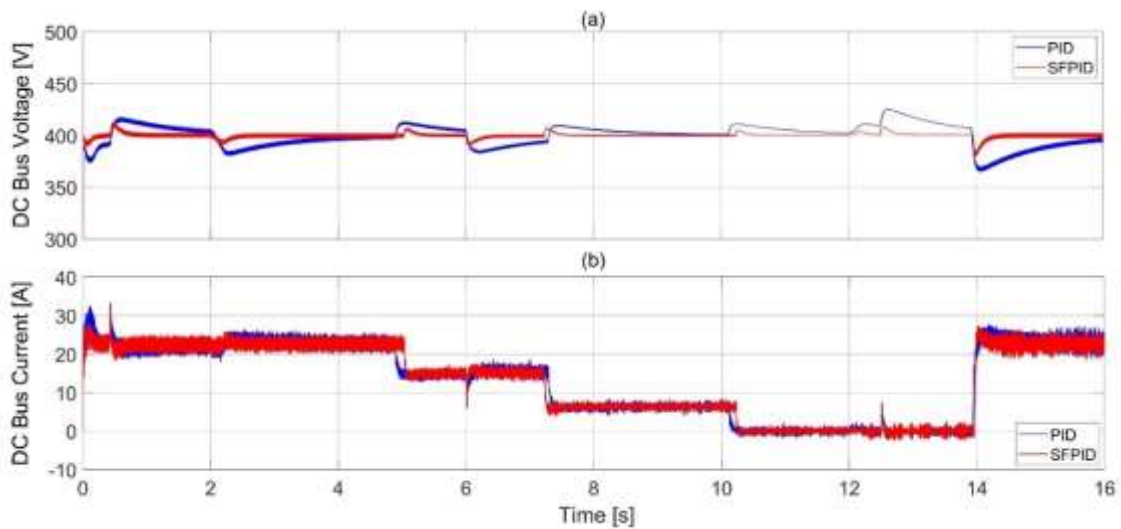**Figure 11.** The power flow of DC MG based on proposed EMS.

Figure 12. DC bus (a) Output voltage and (b) Output current variation graphs.

The graphs of the change in the maximum and RMS values of the load voltage during the simulation process (SFPID) in MG are given in Figure 13. Similarly, the biggest oscillation in the AC bus voltage after the steady-state of the MG occurred at 14s. Considering the maximum and minimum voltage values of the oscillation that continued for 150ms, the voltage regulation results ε_k^+ and ε_k^- are obtained as 0% and -1.74%, respectively (see Figure 13(b)). According to these results, it has been shown that the oscillations in the load voltage are within limits according to the EN 50160 standard [27]. The graph of the change in system frequency during the simulation process in MG is given in Figure 14. The changes in scenarios or load after the stabilization of MG, the maximum oscillation in the system frequency occurred at 14.38 s and lasted for 200 ms (10 cycles). This shows that the oscillations are within the limit values according to EN 50160 standard. Similarly, it has been observed that the SFPID controller greatly reduces oscillations in the system frequency relative to the PID controller.
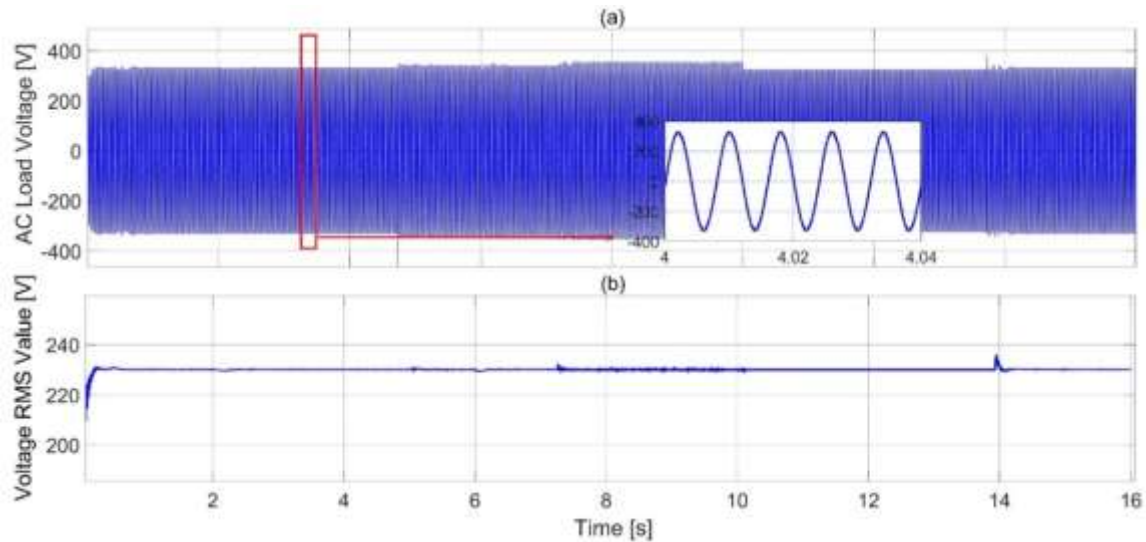

Figure 13. Graph of the AC load voltage change of MG (a) Maximum AC load voltage value (b) AC load voltage RMS value.
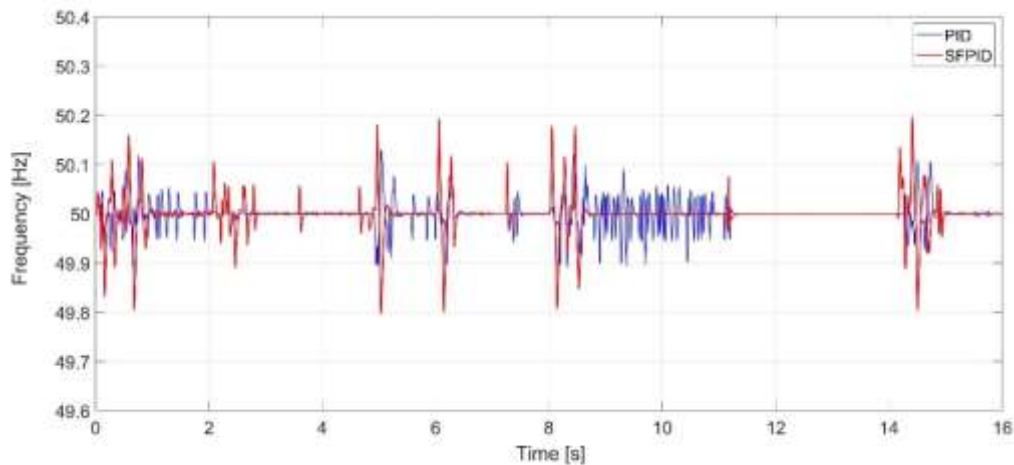

Figure 14. Effect of PID and SFPID controllers on system frequency.

Also, the total harmonic distortion (THD), a measure of the formal proximity between the output waveform and its main component, is one of the performance criteria that measures power quality. As seen from the graphics in Figure 15, THD_V and THD_I in the voltage and current are measured, and it is seen that they are within the limit values according to IEC 61000-4-7 standard [28]. A comparative graph of current and voltage harmonics of SFPID and PID controller is shown in Figure 16. The THD is calculated as 3.54% and 3.29% for voltage and current when using the PID controller in the MG. On the other hand, THD for voltage and current in SFPID is 3.14% and 3.12%, respectively. The results clearly showed that the THD ratio is improved by 9.4% for voltage and 5.17% for current compared to the proposed SFPID controller with the PID controller.
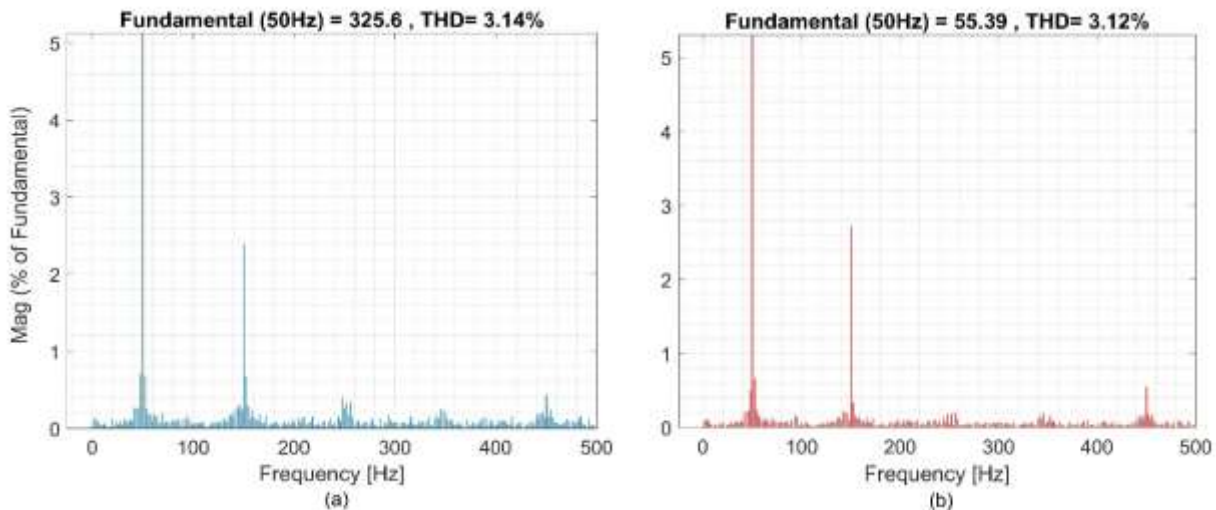
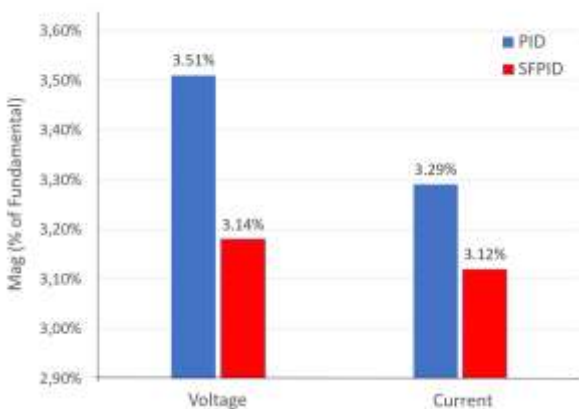**Figure 15.** THD spectrum for SFPID controller (a) Load voltage (b) Load current.

Figure 16. Comparison of voltage and current harmonics

6. Conclusion

In this study, a MG structure consisting of RES with ESS has been developed to operate in standalone and grid-connected modes. The aim is to make maximum use of RES. However, RES and ESS resources may be insufficient to feed the critical load, the worst-case scenario. In this case, MG switches between standalone and grid-connected modes to ensure continuous feed.

In the MG, the SFPID controller is designed for voltage regulation stability compared with traditional PID controllers. Results show that compared to the PID controller, the SFPID controller diminishes overshoot at voltage signal at the system output by 57.14%, shortens settling time by 75.08% and improves rise time by 40%. Thanks to the designed controller and suggested EMS system, the system performance is good and within limit values under all scenarios.

Future work will include a hierarchical control method and hardware implementation for several MGs and ESSs.

Author's Contributions

Ahmet Kaysal: Drafted and wrote the manuscript, performed the result analysis.
Selim Köroğlu: Supervised the manuscript's progress interpretation and helped in manuscript preparation.
Yüksel Oğuz: Assisted in analytical analysis on the structure, supervised the manuscript's progress.

Ethics

There are no ethical issues after the publication of this manuscript.

References

[1].. Merabet, A, Tawfique, KA, Ibrahim, H, Beguenane, R and Ghias, AMYM. 2017. Energy Management and Control System for Laboratory Scale Microgrid Based Wind-PV-Battery. *IEEE Transactions on Sustainable Energy;* 8(1): 145-154.

[2]. Bai, W and Lee, K. 2014. Distributed Generation System Control Strategies in Microgrid Operation. *IFAC Proceedings;* 47(3): 11938-11943.

[3]. El-Bidairi, KS, Nguyen, HD, Jayasinghe, SDG, Mahmoud, TS, Penesis, I. 2018. A hybrid energy management and battery size optimization for standalone microgrids: A case study for Flinders Island, Australia. *Energy Conversion and Management;* 175: 192-212.

[4]. Tummuru, NR, Mishra MK and Srinivas, S. 2015. An Improved Current Controller for Grid Connected Voltage Source Converter in Microgrid Applications. *IEEE Transactions on Sustainable Energy,* 6(2): 595-605.

[5]. Bhosale, R and Agarwal, V. 2019. Fuzzy Logic Control of the Ultracapacitor Interface for Enhanced Transient Response and Voltage Stability of a DC Microgrid. *IEEE Transactions on Industry Applications;* 55(1):712-720.

[6]. Kim, JY, Kim, HM, Kim, SK, Jeon, JH, Choi, HK. 2019. Designing an Energy Storage System Fuzzy PID Controller for Microgrid Islanded Operation. *Energies;* 4(9):1443-1460.

[7]. Vigneysh, T and Kumarappan, N. Stability analysis and dynamic performance enhancement of autonomous microgrid using adaptive fuzzy PI controller, IEEE Congress on Evolutionary Computation (CEC), San Sebastian, 2017, pp. 1199-1206.

[8]. Bayhan, S, Demirbas, S and Abu-Rub, H. 2016. Fuzzy-PI-based sensorless frequency and voltage controller for doubly fed induction generator connected to a DC microgrid. *IET Renewable Power Generation;* 10(8):1069-1077.

[9]. Anantwar, H, Lakshmikantha, BR and Sundar, S 2017. Fuzzy self-tuning PI controller based inverter control for voltage regulation in off-grid hybrid power system. *Energy Procedia;* 117:409-416.

[10]. Saroha, J, Singh, M and Jain, DK. 2018. ANFIS-Based Add-On Controller for Unbalance Voltage Compensation in a Low-Voltage Microgrid. *IEEE Transactions on Industrial Informatics;* 14(12):5338-5345.

[11]. Chauhan, RK, Rajpurohit, BS, Hebner, RE, Singh, SN and Longatt, FMG. Design and analysis of PID and fuzzy-PID controller for voltage control of DC microgrid, IEEE Innovative Smart Grid Technologies, Asia, Bangkok, 2015, pp. 1-6.

[12]. Hu, J, Shan, Y, Xu, Y, Guerrero, JM. 2019. A coordinated control of hybrid ac/dc microgrids with PV-wind-battery under variable generation and load conditions. *International Journal of Electrical Power & Energy Systems;* 104:583-592.

[13]. Jayachandran, M, Ravi, G. 2019. Predictive power management strategy for PV/battery hybrid unit based islanded AC microgrid. *International Journal of Electrical Power & Energy Systems;* 110:487-496.

[14]. Almada, JB, Leão, RPS, Sampaio, RF, Barroso, GC. 2016. A centralized and heuristic approach for energy management of an AC microgrid. *Renewable and Sustainable Energy Reviews;* 60:1396-1404.

[15]. Tuckey, A, Zabihi, S and Round, S. Decentralized control of a microgrid, 19th European Conference on Power Electronics and Applications, Warsaw, 2017, pp. 1-10.

[16]. Feng, X, Shekhar, A, Yang, F, Hebner RE and Bauer, P. 2017. Comparison of Hierarchical Control and Distributed Control for Microgrid. *Electric Power Components and Systems;* 45(10):1043-1056.

[17]. Yazdanian, M and Mehrizi-Sani, A. 2014. Distributed Control Techniques in Microgrids. *IEEE Transactions on Smart Grid;* 5(6):2901-2909.

[18]. Sen, S, Kumar, V. 2018. Microgrid control: A comprehensive survey. *Annual Reviews in Control;* 45:118-151.

[19]. Rajesh, KS, Dash, SS, Rajagopal, R, Sridhar, R. 2017. A review on control of ac microgrid. *Renewable and Sustainable Energy Reviews;* 71:814-819.

[20]. Unamuno, E, Barrena, JA. 2015. Hybrid ac/dc microgrids—Part II: Review and classification of control strategies. *Renewable and Sust1ainable Energy Reviews;* 52:1123-1134.

[21]. Ziouani, I, Boukhetala, D, Darcherif, AM, Amghar, B, El Abbassi, I. 2018. Hierarchical control for flexible microgrid based on three-phase voltage source inverters operated in parallel, *International Journal of Electrical Power & Energy Systems;* 95:188-201.

[22]. Mohamed, AA, Elsayed, AT, Youssef, TA, Mohammed, OA. 2017. Hierarchical control for DC microgrid clusters with high penetration of distributed energy resources. *Electric Power Systems Research;* 148:210-219.

[23]. Wu, B, Lang, Y, Zargari, N and Kouro, S. Power Conversion and Control of Wind Energy Systems; Hoboken, NJ, USA: John Wiley & Sons, 2011.

[24]. Rashid, MH. Power Electronics Devices, Circuits and Applications, Prentice-Hall, Englewood Cliffs, New Jersey, 2003.

[25]. Bingi, K, Ibrahim, R, Karsiti MN and Hassan, SM. Fuzzy gain scheduled set-point weighted PID controller for unstable CSTR systems, IEEE International Conference on Signal and Image Processing Applications, 2017, pp. 289-293.

[26]. Santos, P, Fonte P and Luis, R. Improvement of DC Microgrid Voltage Regulation Based on Bidirectional Intelligent Charging Systems, 15th International Conference on the European Energy Market, Lodz, 2018, pp. 1-6.

[27]. Seme, S, Lukač, N, Štumberger, B, Hadžiselimović, M. 2017. Power quality experimental analysis of grid-connected photovoltaic systems in urban distribution networks. *Energy,* 139:1261-1266.

[28]. Oliveira, WR, Anésio, LF, Filho, JC. 2019. A contribution for the measuring process of harmonics and interharmonics in electrical power systems with photovoltaic sources. *International Journal of Electrical Power & Energy Systems;* 104:481-488.